Powder Densification. 1. Particle–Particle Basis for Incorporation of Viscoelastic Material Properties

SUSAN K. LUM*,† AND WENDY C. DUNCAN-HEWITT†,‡

Contribution from *Faculty of Pharmacy, University of Toronto, 19 Russell Street, Toronto, Ontario, Canada M5S 2S2.*

Received January 9, 1998. Accepted for publication November 9, 1998.

Abstract □ The present investigation was undertaken to examine the basic unit of densification: the particle–particle indentation. The true interparticle contact area that is established during densification ultimately determines the quality of the tablet compact. By examining the interfacial contact between mutually indenting viscoelastic particles, the process of contact evolution may be represented in mathematical form through extension of the classical Hertzian elastic contact description to encompass material viscoelastic terms. In this way, the time-dependent response of materials to applied loads may be addressed explicitly. The effects of rates of applied loading and maximum load levels were also considered. This analysis was based on viscoelastic stress data collected using an instrumented Instron analyzer during the densification of PMMA/coMMA, a pharmaceutical polymeric coating material. A crossed cylinder matrix compaction geometry was used to simulate the geometry of two mutually indenting spherical particles. Numerical and graphical solutions delineating the relationship between contact area evolution and the prescribed loading force are presented. This particle–particle description of the contacting interface serves as a unit basis for describing the entire powder bed. The powder bed may ultimately be modeled as a collection of these particles in contact.

Introduction

Oral administration is the most common route of drug delivery for systemic circulation. The tablet is the leading oral form; it's simplicity, portability, and economic value enhances patient compliance. Tablets exist in diverse forms, ranging from conventional disintegrating forms to advanced modified-release systems, but all are formed through a common pathway, namely, through powder densification.

Powder densification consists of sequential and concurrent processes where particles are brought into intimate contact, interparticulate bonds are formed, and dimensional changes occur as a result of stress redistribution. Time-dependent phenomena inherent in these processes may govern the ultimate quality of the compact produced. Permanent densification occurs when stress exceeds the elastic strain limit of a given material. The extent of this nonrecoverable deformation depends on the time in which the applied stress exceeds this material yield stress. It is viscoelastic theory that serves to quantitate this time dependence and provide a description of the relationship between the strain rate of the material in a plastic state and the stress required to produce that strain rate.

The compaction of powders is a complex process. The rate at which compacts are formed determines the final tablet strength and viability.[1−4] With the advent of modern processes, the high speeds of compaction emphasize the time-dependent component of material behavior. This complexity is reflected in the large-scale manufacturing of tablets where problems of low tablet strength, capping and sensitivity to material batch variability exist and are translated into costly overruns. Resolution of these problems often involves multiple formulation adjustments based on empirical knowledge rather than the reasoned use of physical data; improving the theoretical understanding of the compaction process would enable a more rational approach to the formulation of tablets.[5]

It is conjectured that problems arise during tablet production as a consequence of viscoelasticity combined with poor interparticle bonding. The amount of elastic recovery of the particles depends on the release of elastic strain during decompression and tends to disrupt interparticle bonds. This stress relaxation is a function of the viscoelasticity of the material, which in turn is influenced by the speed of compression and decompression. At high compaction speeds, the internal stress after compaction is high and the propensity of the material for elastic recovery is considerably higher than at low compaction speeds.

Existing approaches to assess powder compaction have mainly tried to quantify compression in an empirical form. The equations proposed to empirically fit compaction data with parameters such as punch and die wall stresses and tablet porosity[6−9] offer little insight into the physical basis for particle interaction. Therefore, they remain descriptive rather than predictive of powder densification.

A predictive model of compaction must explicitly incorporate material viscoelastic terms into a working description of densification. Analytical models that describe densification from the deformation of particles serve to facilitate the selection of production process parameters such as pressure, temperature, and time. The present investigation was undertaken to examine the basic unit of densification: the particle−particle interaction. By defining the contact between mutually indenting viscoelastic particles, the compact may ultimately be modeled as a collection of these particles in contact and in this way address the time-dependent response of materials to applied loads.

Rationale

In random close packing of a powder bed, point contacts exist between adjacent particles. The density of the powder increases through processes that flatten these contacts between particles. The degree of interparticle bonding and bond strength, which which determines the ultimate quality of a tablet, is assumed to be largely governed by the magnitude of the true interparticle contact area created during densification. This process of contact evolution may be represented in mathematical form through amelioration of the classical Hertzian elastic contact description to encompass material viscoelastic terms. In this way, a

* Author to whom all correspondence should be sent. Telephone: (416) 978−2889. Fax: (416) 978-8511. E-mail: susan.lum@utoronto.ca.
† Faculty of Pharmacy.
‡ Consultant, Grian Facilitations, http://www.grian.com, 1929 Howard Drive, Amarillo, TX, 79106.

10.1021/js980010m CCC: $18.00
Published on Web 01/15/1999

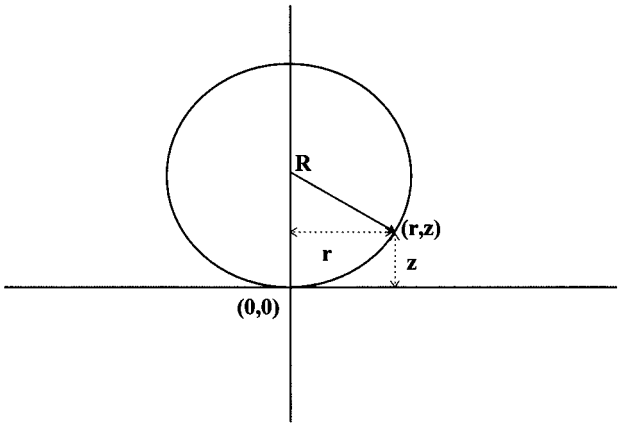

Figure 1—Schematic for the 2-D projection of a contact area. The equation of a translated circle with respect to the origin in the *x*–*y* Cartesian coordinate plane at a point designated (*r*,*z*) (where *R* is the radius of the circle) and where one assumes that $2R \gg z$ is $\therefore z \cong r^2/2R$. This is valid for cases where deformations are small.

quantitative measure of the contact deformation between mutually indenting viscoelastic particles may be defined.

Theoretical Section

The time-dependent stress and indentation behavior of the test matrixes were modeled in terms of a standard linear viscoelastic rheological form transposed into the classical elastic description of contact. Components of the theory underlying this contact deformation may be found interspersed in the literature for specific geometries.[10,11] The following derivation of the theory describing the contact between spherical particles of a viscoelastic material, as applied to these studies, is developed in detail for the integral understanding of the resultant model.

Boundary Conditions for the Deformation between Two Spherical Bodies in Contact—The geometry of the surface of undeformed spheres near the center of contact are smooth surfaces that can be described with sufficient accuracy, as shown in Figure 1, by

$$z_1 = \frac{r^2}{2R_1} \qquad z_2 = \frac{r^2}{2R_2} \tag{1}$$

and the mutual distance between points is

$$z_1 + z_2 = r^2\left(\frac{1}{2R_1} + \frac{1}{2R_2}\right) = \frac{r^2(R_1 + R_2)}{2R_1R_2} \tag{2}$$

If the spheres are compressed together by a normal force *P*, there will be a local deformation near the point of contact producing contact over a small surface with a circular boundary, hence, the surface of contact arises.

Let w_1 and w_2 be the deformations of the two spheres owing to the contact pressure, *a* the radius of the contact region, and α be the total distance of approach of the two spheres from the state of point contact. The deformed configuration is shown in Figure 2. The condition

$$w_1 + w_2 = \alpha - (z_1 + z_2) \tag{3}$$

is to be satisfied at each point in the contact region. By eq 2

$$w_1 + w_2 = \alpha - \left(\frac{r^2(R_1 + R_2)}{2R_1R_2}\right) \tag{4}$$

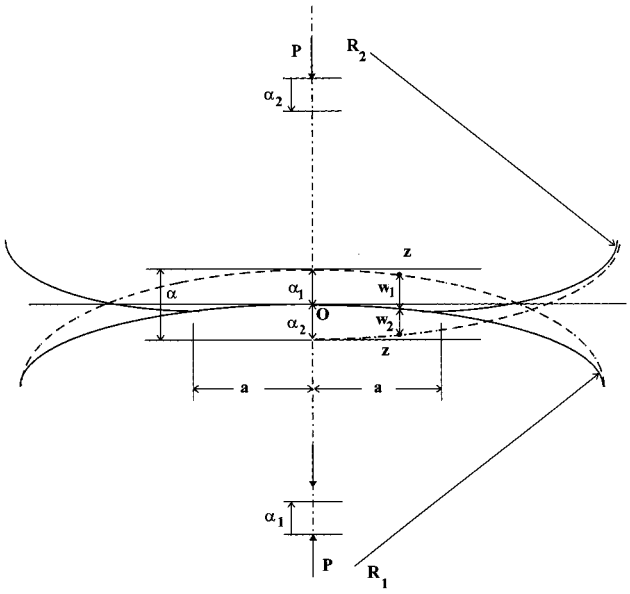

Figure 2—Schematic for the deformation between two spheres from the state of point contact. The deformed configuration is shown with dotted lines indicating the distance of approach of either sphere.

If points lie outside the contact area so that they do not touch it follows that

$$w_1 + w_2 > \alpha - \left(\frac{r^2(R_1 + R_2)}{2R_1R_2}\right) \tag{5}$$

from geometry alone.

Pressure between Two Spheres in Contact—The distribution of pressure transmitted between the two bodies at their surface of contact must be such that the resultant displacements normal to that surface satisfy eq 4 within the contact area and eq 5 outside it. Because the contact region is comparatively much smaller than the dimensions of the bodies ($r \ll R_1$ and R_2), the relation between the surface deflection of each body and the contact pressure can be represented approximately by the solution for surface deflection of a semi-infinite body with pressure distributed on part of its surface. The errors incurred by assuming that the spheres are half-spaces are smaller than those due to the assumption of infinitesimal strains.[12]

Let $a(t)$ be the radius of the contact region and $\alpha(t)$ the total distance of approach. For a given concentrated force acting on a boundary plane of a semi-infinite solid, the displacement is given by[11]

$$w_{z=0} = \frac{q(1 - v^2)}{\pi E r} \tag{6}$$

where *w* is the total displacement, *q* is the intensity of pressure between the bodies in contact, *v* is the Poisson's ratio, *E* is the elastic modulus, and *r* is the distance from the center.

In the case of an uniform load distributed over the area of a circle of radius *a*, if a point D is within the loaded area, the displacement produced is found by superposition. The load on the shaded element in Figure 3 which represents the surface of contact, is $qs\mathrm{d}\psi\mathrm{d}s$. The displacement in the direction of the load is then

$$\frac{(1 - v^2)q}{\pi E}\frac{s\mathrm{d}\psi\mathrm{d}s}{s} = \frac{(1 - v^2)q}{\pi E}\mathrm{d}\psi\mathrm{d}s \tag{7}$$

If there is no pressure between the bodies, we have contact

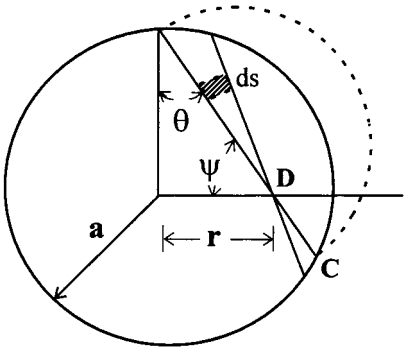

Figure 3—Sketch of a circular contact region of radius *a*. This is the surface of contact over which an uniform load has been distributed.

at one point O. Points D and C are on a meridian section of the spheres, on the plane tangent at O, at a very small distance r (r is small in comparison with R_1 and R_2) from the axis.

The total deflection of a point on the circular contact surface is then obtained by double integration

$$w = \frac{(1 - \upsilon^2)}{\pi E} q \int\int \mathrm{d}\psi \mathrm{d}s \tag{8}$$

because the length of the cord indicated by $bc = 2r = 2a \cos\theta$ and because $r = a \cos\theta = \sqrt{a^2 - r^2 \sin^2\psi}$ the area of the circle $= \pi r^2 = \pi(a^2 - r^2 \sin^2\psi)$ and ψ varies from 0 to $\pi/2$ (see *Appendix I*):

$$\therefore w = \frac{(1 - \upsilon^2)}{\pi E} q \pi \frac{\pi}{4}(2a^2 - r^2) \tag{9}$$

Expressions for the Displacement and Radius of the Contact Surface— Let $(1 - \upsilon^2)/\pi E = k_1 + k_2$ and assume a Hertzian pressure distribution wherein the scale[11] representing the pressure distribution is the constant q_0/a. Thus from eqs 4 and 9, for two same sized spheres in contact,

$$\therefore (k_1 + k_2)\frac{q_0}{a}\frac{\pi^2}{4}(2a^2 - r^2) = w = \alpha - \frac{r^2}{R} \tag{10}$$

Which is then solved by making a term-by-term equivalence between the left- and right-hand sides of this equation

$$\therefore \alpha = \frac{(k_1 + k_2)}{2} q_0 \pi^2 a \tag{11}$$

And because

$$\frac{1}{R} = \frac{(k_1 + k_2)}{4a} q_0 \pi^2 \tag{12}$$

$$\therefore a = \frac{(k_1 + k_2)}{4} q_0 \pi^2 R \tag{13}$$

By adopting the Hertzian pressure distribution assumption (see *Appendix II*),

$$q_0 = \frac{3P}{2\pi a^2} \tag{14}$$

which relates the maximum pressure, q_0, to the loading force, P. We thus find

$$a^3 = \frac{3}{8}\pi(k_1 + k_2)PR \tag{15}$$

by substituting eq 14 into eq 13.

Extension to the Viscoelastic Case—Solutions to the contact problem must accommodate mixed boundary conditions, assigned depending on whether the point in question lies inside or outside of the contacting region. Within the contacting area, the sum of the surface displacements of the two bodies must satisfy constraints to ensure perfect contact, whereas the surface traction must vanish outside of the contact area.

At first reckoning it may appear that Laplace transforms could be useful in addressing the viscoelastic or time-dependent contact case by removing the time variable in the governing equations and boundary conditions. Hence, the problem may be reduced to a corresponding elastic problem with the Laplace transform variable as a parameter. The desired viscoelastic solution would then be an inversion of the solution to the corresponding elastic case.

Viscoelastic contact regions, however, vary with time. Some points initially outside of the region of contact may fall later into the contacting region as the result of the growing indentation area. For these points, neither the traction nor the displacement may be prescribed completely throughout the development of the problem; the transform method may not be used directly to supply a solution to the problem.

Notwithstanding, it has been shown through inductive reasoning that the contact problem in elasticity may be generalized to include the contact of viscoelastic bodies with a restriction that the indentation must be monotonically increasing. Lee and Radok[13] treated a range of problems that fall outside the scope of the transform method by taking a family of solutions of the elastic problem with the parameter time, with the same boundary conditions as the viscoelastic problem, and replacing the elastic constants with the appropriate viscoelastic operators in the expression for stress components. The results comprise tractable mathematical equations for evaluating the stress components for the viscoelastic body.

In the elastic case of mutual indenting spheres, as shown in eqs 11–15, the normal contact pressure $p(r,t)$ of the assumed elastic half space is the relation[14,15]

$$p(r,t) \propto \frac{4}{\pi R}\frac{G}{1 - \upsilon}\sqrt{a^2(t) - r^2} \tag{16}$$

where G is the shear modulus, υ is the Poisson's ratio, and $a(t)$ is the contact area radius. Time appears only as a parameter prescribing the current radius of contact in this quasistatic approach. The elastic constants do not contain time explicitly and so when they are replaced by general linear operators, the solution at any time t depends solely on the instantaneous value of the boundary condition and not on the history of the process.

The viscoelastic counterpart of this Hertzian problem in elasticity as deduced from the elastic solution is then

$$P[p(r,t)] = \frac{4}{\pi R} Q[f(r,t)] \tag{17}$$

where $f(r,t) = \sqrt{a^2(t) - r^2}$, P, and Q are linear operators in the time variable.

The problem is now defined by a normal surface traction $p(r,t)$ and a zero shear traction and is amenable to analysis by the Laplace transform procedure. The transformed

surface pressure

$$\bar{p}(r,s) = \frac{4}{\pi R}\frac{\bar{Q}}{\bar{P}}\bar{f}(r,s) \tag{18}$$

is then related to $\bar{Q}$, $\bar{P}$, the transformed form of the operators. If integral operators are used, the convolution theorem then determines the transformed form.

This procedural manipulation of the operators is valid as long as the contact area does not decrease. In any physically reasonable contact problem of this type, to satisfy the restriction of the Hertz theory, the region of contact will be limited to a finite area. The transformed pressure given by eq 18 is thus nonzero only inside this maximum region of the contact. If the radius of contact increases to a maximum and then decreases to zero, then the normal deflection of the entire surface would reduce to zero, contradicting the reality of viscoelastic material behavior. Delayed elastic and viscous components of strain would be expected to leave a residual indentation after contact has ceased.

The reason for this paradoxical result is that if $a(t)$ passes through a maximum and decreases, then the corresponding $p(r,t)$ usually passes through zero and takes on negative or tensile values. When $a(t)$ then decreases, a residual tensile surface traction is left at the points formerly in the contact region, which violates the contact condition that outside the current region of contact the surface traction should be zero. This dilemma does not arise with nondecreasing $a(t)$ because the zero initial condition for all earlier times guarantee zero traction outside the region of contact.

What follows is a derivation of the formula for the extension of the contact problem to linear viscoelastic spheres. To reduce the complexity of the problem, a number of assumptions were adopted. It was assumed that both bodies in contact were isotropic, homogeneous, and linearly viscoelastic. The material properties were characterized by creep or relaxation functions. Moreover, the surfaces were considered smooth to neglect the effect of friction. Small strains were assumed, as evidenced in the preceding derivations where the area of contact is small in comparison with the dimensions of the contacting bodies. The indentation area should furthermore increase monotonically with time. And finally, shear and dynamic and intermolecular force effects were neglected.

Rheological Model for Viscoelastic Case—The behavior of viscoelastic materials under uniaxial loading may be represented by means of conceptual models composed of elastic and viscous elements. Such rheological forms are useful as analogues for stress and strain. The basic elements of springs and dashpots also assists in the conceptualization of the material behavior.

An ideal helicoidal spring element would be perfectly linear and massless, representing Hooke's Law:

$$\sigma(t) = E\epsilon(t) \tag{19}$$

where E is the modulus of elasticity with dimension (force/length^2). The spring has a creep function $H(t - \tau)/E$ and a relaxation function $EH(t - \tau)$. The dashpot as an ideal viscous element extends at a rate proportional to the force applied, according to Newton's Law:

$$\dot{\epsilon}(t) = \frac{\sigma(t)}{\eta} \tag{20}$$

where $\dot{\epsilon} = \partial\epsilon/\partial t$ is the rate of strain and η is the viscosity coefficient with dimension (force × time × length^{-2}).

Different combinations of springs and dashpots afford flexibility in portraying different responses. Whereas simple

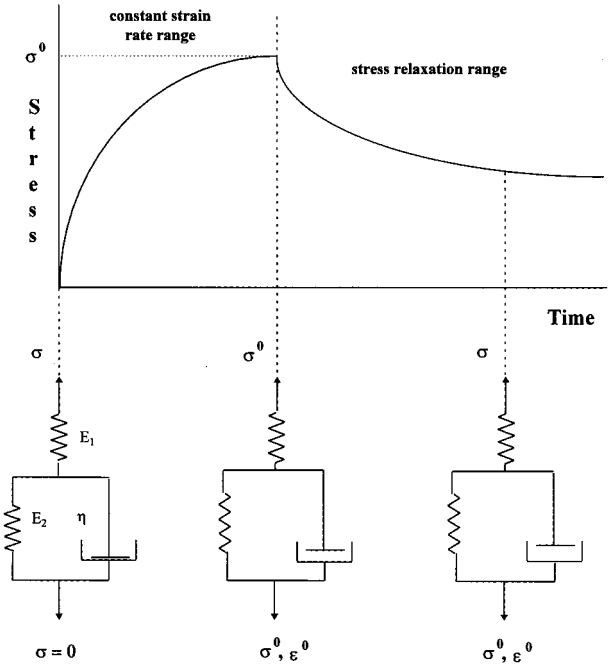

Figure 4—Illustration of the stress–time relation in association with a standard three-parameter rheological model.

models are inadequate representations of real viscoelastic behavior, a three-parameter, standard model consisting of two springs and a dashpot has successfully portrayed real material behavior.[17,18] A standard model was thus employed in the extension of the description of particle contact to the viscoelastic case.

In operational form, this standard model (Figure 4) appears as

$$E_1\eta\dot{\epsilon} + E_1E_2\epsilon = \sigma(E_1 + E_2) + \eta\dot{\sigma} \tag{21}$$

By integrating over a strain history $\epsilon(t)$

$$\therefore \sigma(t) = \epsilon(t)\frac{E_1E_2}{E_1 + E_2} + \frac{E_1^2}{E_1 + E_2}\int_0^t e^{-\frac{(t-\tau)(E_1+E_2)}{\eta}}\dot{\epsilon}(\tau)d\tau \tag{22}$$

Wherein the creep function is

$$\phi(t) = \frac{1}{E_1} + \frac{1}{E_2}(1 - e^{-\frac{tE_2}{\eta}}) \tag{23}$$

and the relaxation function is

$$\Psi(t) = E_1e^{-\frac{t(E_1+E_2)}{\eta}} + \frac{E_1E_2}{E_1 + E_2}(1 - e^{-\frac{t(E_1+E_2)}{\eta}}) \tag{24}$$

Linear Viscoelasticity—Many materials, notably polymers, exhibit time-dependent behavior in their relationships between stress and strain. The common features of a three-parameter or standard solid viscoelastic behavior includes an initial elastic response to an applied or eliminated stress, a delayed elastic response, and a permanent strain that is acquired through the action of creep.

Linear viscoelastic relationships are valid for small strains and assume the principle of superposition holds:[16] a stress history of

$$\sigma(\tau) = \sigma_1(\tau) + \sigma_2(\tau) \qquad \tau \ni (\tau_0,t) \tag{25}$$

corresponds to a strain history of

$$\epsilon(\tau) = \epsilon_1(\tau) + \epsilon_2(\tau) \quad (26)$$

Materials often exhibit linear behavior at low stresses and nonlinear viscoelastic behavior at high stresses.

The stress–strain relations for a linear viscoelastic material are commonly expressed as a relaxation function, $\Psi(t)$. This function, as already deduced from a standard spring-dashpot model, expresses the stress response to a step change in strain.

Viscoelastic Case Analysis—As the preceding contention shows, the interfacial description of two linearly viscoelastic spheres in normal contact may be described mathematically by replacing the elastic constant of the elastic solution by the integral operator from the viscoelastic stress–strain relations. For simplicity, the case of an isotropic, homogeneous, incompressible, and linearly viscoelastic material in the absence of shear is considered. These stipulations facilitate the analytical solution for the case of indentation of smooth viscoelastic spheres; the three-dimensional constitutive equations can be simplified to allow for the application of one pair of viscoelastic operators, p and q, as described by the stress–strain differential equation (see *Appendix III*):[19]

$$\left(\sum_0^m p_k \frac{\mathrm{d}^k}{\mathrm{d}t^k}\right)\sigma = \left(\sum_0^n q_k \frac{\mathrm{d}^k}{\mathrm{d}t^k}\right)\epsilon \quad (27)$$

The condition of very small strains permits the use of linear viscoelastic theory, although it is not a necessary restriction in the treatment detailed by Lee and Radok.[13] The elastic constants can be replaced by viscoelastic terms in the method of analysis for contact of smooth bodies of arbitrary linear viscoelastic materials, just as the Hertz solution applies for arbitrary smooth elastic bodies.[13] The form of the viscoelastic operator can be expressed in terms of the creep compliance or relaxation function found in eqs 23 or 24.

Thus, the contact between spherical particles may be described by substituting the viscoelastic operator ($\Psi(t)$, eq 24) for the elastic constants in the elastic solution found in eq 15. We then have

$$a^3(t) = \frac{3}{8}\pi R \int_0^t \left\{\frac{1}{E_1} + \frac{1}{E_2}\left(1 - \mathrm{e}^{-\frac{(t-t')E_2}{\eta}}\right)\right\}\frac{\mathrm{d}}{\mathrm{d}t'}P(t')\mathrm{d}t' \quad (28)$$

and

$$p(r,t) = \frac{\pi R}{4}\int_0^t \left\{E_1 \mathrm{e}^{-\frac{t-t'}{\tau}} + \frac{E_1E_2}{E_1+E_2}\left(1 - \mathrm{e}^{-\frac{t-t'}{\tau}}\right)\right\} \times \frac{\mathrm{d}}{\mathrm{d}t'}(a^2(t') - r^2)^{1/2}\,\mathrm{d}t' \quad (29)$$

where

$$\tau = \frac{\eta}{E_1 + E_2} \quad (30)$$

is a descriptor of viscoelastic material behavior. These equations, therefore, delineate then an explicit relation between contact area evolution and the applied contact force; a relation that will form the basis for the superposition of such contacts in summation over the entire powder bed.

Experimental Section

Instrumentation—An Instron 4206 stress–strain analyzer, housed in a climate-controlled room (T = 26 °C, RH = 45 ± 6%), was instrumentized through the addition of a 12-bit 10 mV unipolar A/D data acquisition board (PC-LPM-16, National Instruments, Austin, TX). With an op-amp added in line, the voltage signals from up to 8 channels exiting the control console were digitized for collection on a 486-DX clone. The commercial software provided with the board was modified to facilitate signal collection; the testing force was monitored at 250 points per second and averaged over 25 points to reduce spurious fluctuations associated with noise.

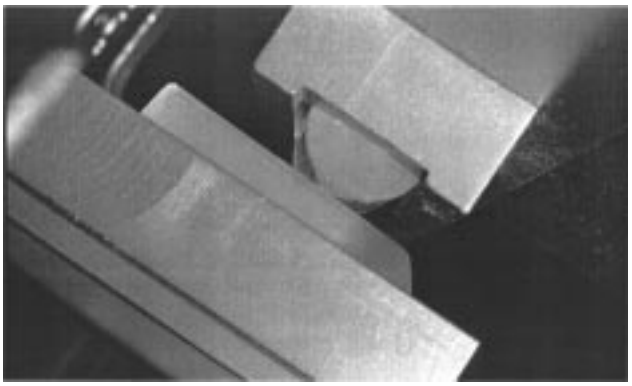

Figure 5—PMMA/coMAA cylinders displayed in crossed cylinder compaction geometry. Matrixes are mounted in stainless steel holders, which in turn are clamped to the platens within the Instron assembly.

Rods to be tested were oriented either axially or radially in stainless steel holders that were machined to fit the contour of the halved rods and that clamped directly onto the upper and lower base platens of the Instron. The test samples were held in compression and the forces experienced by the samples were measured as that transmitted by the load cell. The configuration is displayed in Figure 5.

The 5 kN, 150 kN reversible load cells, and the Instron itself were serviced and calibrated by the source company (Instron) prior to beginning experimental testing. Signal output to the board was calibrated to the force displayed on the console by verifying emitted voltages with a digital multimeter (Beckman 4.5 digit model 800). This calibration extended beyond the experimental applied forces associated with the displacement measurements and served to establish both the calibration factor and the linearity of response ($r^2 > 0.999$).

Materials—Inhibitor-free methyl methacrylate (MMA; Fischer, lot no. 911696) and methacrylic acid (MA; Aldrich, lot no. 07015EZ) were used as they were received. 2,2′-Azobisisobutyronitrile (AIBN; Analychem Corp. Ltd., Markham, Ontario, lot no. 413286) was recrystallized from isopropyl alcohol, and the HPLC grade tetrahydrofuran (THF) (Fischer, lot. no. 904140) was freshly distilled prior to use.

Specimen Synthesis—Ideal contact between two spheres is difficult to achieve experimentally, so the geometry was approximated by the contact of crossed cylinders at 90°. Poly(methyl methacrylate)/comethacrylic acid (PMMA/coMAA), an amorphous acrylic polymer similar to the commercial pharmaceutical Eudragit, was chosen as the model material for study. Although the flow and material properties of PMMA alone are well documented, the copolymer material is more commonly employed in pharmaceutical coating and encapsulation.

PMMA/coMAA cylinders were prepared by free radical bulk polymerization of a 1:1 mole ratio mixture of inhibitor-free MMA and inhibitor-free MAA using recrystallized AIBN as the initiator. The mixture was deaerated by repeated freeze thawing under an argon blanket, and the polymerization was carried out in sealed 13-mm diameter glass molds under Argon at 25°C for 4 weeks (Atmos environmental bag, Sigma Chemical Company, St. Louis, MO). During solidification, the molds were continuously agitated to minimize porosity from trapped gas bubbles (Psycrotherm Incubator shaker model R-27, ser. 8695; NewBrunswick Scientific Company Inc., New Brunswick, NJ). The resulting cylinders were purified by extracting any residual monomer, side products, or initiator by Soxhlet reflux (MeOH/water, 60/40 by volume). Rods were halved longitudinally, polished, and used together as the opposing upper and lower contact elements in compression (wire saw and diamond impregnated wire blades, 0.010" diameter, South Bay Technology, San Clements, CA; Crystal Bay crocus abrasive

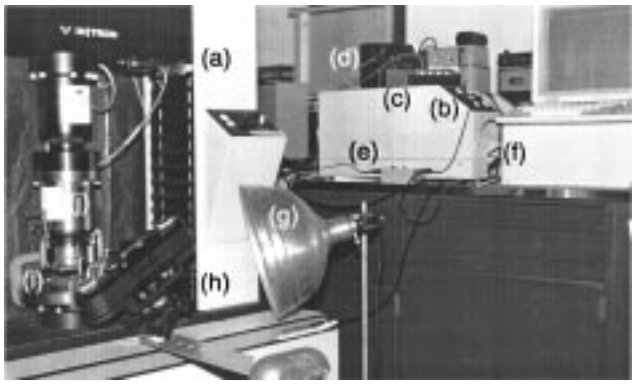

Figure 6—Instrumentation associated with compressional loading of polymer matrixes and concomitant photomicroscopy survey of contacting region: (a) Instron 4206; (b) Instron control console; (c) op-amp for signal transduction; (d) timing relay; (e) single switch or continuous relay; (f) 486DX for automated data acquisition and control, equipped with A/D board; (g) contrast illumination; (h) bulk loaded camera driven through electronic relay; (i) samples mounted within platens; and (j) reversible load cell.

cloth, 3M Canada Inc., London, Ontario, Canada). A nominal aspect ratio (length-to-diameter ratio) of at least 2:1 was chosen to avoid complications of edge effects or barreling during compression. Care was also taken that the material did not come into contact with water or any contaminant while the specimens were being prepared or during subsequent handling and testing; mainly by storage with desiccant under an argon blanket. The samples for this study were annealed at 170 °C for 2 h prior to deformation testing.

Polymer Characterization—Changes in material morphology and properties among sample matrixes were controlled by annealing and monitored by microhardness and acoustic testing as described elsewhere.[20] The mean diameters of five indentations per sample were used to calculate the Knoop hardness values and the corresponding elastic moduli, which averaged 11.3 ± 3.9 MPa and 5.67 ± 0.2 GPa, respectively, at 25 °C. The copolymer was further characterized by a variety of means as reported previously: [21] solid density measurements at various temperatures by stereopycnometer yielded $\rho = 1.20$ g/mL at 20 °C (SE = ±0.001 g/mL), differential scanning calorimetry scans showed a $T_g \sim 175$ °C and no evidence of crystallinity, copolymer composition was checked by Fourier transform infrared (FTIR) spectroscopy, and the viscosity average and weight average molecular weight were determined, respectively, by capillary viscometry and low angle laser light scattering, $M_w \sim 5 \times 10^5$.

Contact Deformation—Compaction between two cylinders was performed on the instrumentized Instron already described at four rates ranging from 1 to 10 mm/min and at four loads ranging from 3.0 to 4.5 kN. Stress relaxation was also monitored for 20 min after the peak load was achieved. At least three runs were performed at each load level and nominal strain rate. The contacting surface radius was determined concomitantly by optical means.

Growth of the contact area, produced by the forces applied to the mutually indenting rods, was measured photomicroscopically with an automated camera system equipped with a custom 10-mm microlens. The camera was mounted on a tripod parallel to the interface of the contacting matrixes, loaded with bulk film, and driven frame by frame by synchronized relay (Nikon F-250, Nippon Kogaku, Japan; TMAX 100 black and white film, Kodak, Canada; Nikon film winder cassette; Intervalomeer HN−I with single or continuous relay and motor driver, HN1 Anglophoto Ltd, Montreal). The timing of the relay and subsequent shutter interval was checked by stopwatch and matched to the timing of the force-data acquisition. High contrast photos were taken of the contact zone at 90° to the axis of compression at 1 s intervals, processed, magnified, and measured (Mitotuyo 500−133 vernier calipers). The instrumentation is depicted in Figure 6 for purposes of visualization. The data from these measurements were analyzed according to methods described next.

Data Analysis—*Force−Time Signal*—Below 0.6 kN on all preliminary and subsequent curves, a distortion was evident in the applied force that produced a replicate kink in the force−time plot across all applied loads and nominal strains. This artifact was attributable to the operational system of the Instron employed. Although hydraulically loaded systems provide an instantaneous force to the testing area, screw-loaded systems must overcome the give or stiffness of the machine before actual loading occurs. The screw-loaded Instron 4206 was employed because of its availability.

The force−time signals relayed to file were smoothed at <0.6 kN. The 0.6 kN value itself corresponds roughly to the 7.5% limit of sensitivity specification for the 5 kN reversible load cell employed for the majority of the experimental runs. Fortran subroutines were written to handle the data sets. The collected force signals were converted by the calibration already noted fitted to a power form by nonlinear regression following a Marquardt algorithm, and back extrapolated at 0.6 kN to the proper abscissa point to offset the time-lag associated with the screw loading.

In the nonlinear least-squares fitting, a chi squared merit function was defined and a best-fit parameter determined by its minimization. The iterative minimization proceeded from trial values input for the parameter following a Marquardt subroutine method (template[22]), which varies smoothly between the extremes of the inverse-Hessian method and the method of steepest descent. Several initial values were iterated through to safeguard against convergence onto a local rather than a global minimum. For each of the 4 × 4 matrix experiments repeated in triplicate, the best fit was assessed by minimization of the sum of squares, comparison of the multiple correlation coefficient, and examination of the residuals and the standard error associated with the estimate of the coefficient to the power form.

The resultant equations for the 4 × 4 design, of the form force $P(\text{time}) = \text{coefficient}*(\text{time-lag time})^{\text{power}}$ were amassed and assessed for correlations with the prescribed load levels and nominal strain rates. Multiple linear regression was applied in both forward and backward substitution forms for various combinations and permutations of the load level and crosshead rates. The best aggregate description was determined on the basis of assessment of the adjusted R, the standard error of the estimate, and the mean square residuals.

Radial Growth Data—The measured contact radii were normalized by the initial apparent contact radius that occurs as a result of the weight of the upper rod resting on the lower. Although the timing relay between photos was calibrated by stopwatch, minor variations accruing from the finite shutter speed time necessitated checking the timing intervals between radii measurements. This calculation was accomplished given the peak force time signal and the number of frames advanced. Accounting also for measurement magnification, and the lag-time associated with screw loading, the radii data provided normalized radius growth with time curves in triplicate for the 4 × 4 design (for various nominal strain rates and ultimate loading levels).

Calculation of Material Viscoelastic Parameters—Relaxation or creep compliance functions are traditionally measured by creep tests, in which constant strain rates or stresses are applied to achieve constant stresses or strain rates, respectively, at various elevated temperatures. These measurements require long loading times to reach steady state, which may change either the geometry of the specimen or the microstructure and hence the stress−strain relation. Changes such as these are especially important in porous powder materials which tend to densify during indentation creep testing.

Following the method of Hsueh,[23,24] the viscosity and the two elastic moduli of a three-parameter model constructed to represent a viscoelastic material were determined from the experimental stress−time curve generated from short-term loading at a constant strain rate ($\dot{\epsilon}_0$) followed by a period of stress relaxation. By decomposing the stress−time curve into the applied periods of strain, then for $\dot{\epsilon} = \dot{\epsilon}_0$,

$$\sigma(t) = \left(\frac{E_1}{E_1 + E_2}\right)^2 \eta\epsilon_0[1 - \exp^{-\frac{(E_1 + E_2)}{\eta}t}] + \frac{E_1E_2}{E_1 + E_2}\dot{\epsilon}_0 t \qquad (31)$$

During the stress relaxation phase, $\dot{\epsilon} = 0$ and

$$\sigma(t) = \sigma_\infty + (\sigma_f - \sigma_\infty) \exp^{-(t - t_i)\frac{(E_1 + E_2)}{\eta}} \qquad (32)$$

where

$$\sigma_\infty = \frac{E_1 E_2}{E_1 + E_2}\dot{\epsilon}_0 t_f$$

$$\therefore \sigma(t) = A[1 - \exp^{-\frac{t}{\tau}}] + \sigma_\infty \frac{t}{t_f} \quad (33)$$

for $t > t_f$, where $\tau = \eta/(E_1 + E_2)$, and $A = (E_1/E_1 + E_2)^2 \eta \dot{\epsilon}_0$.

Examination of the stress–time curve provides estimates for t_f, the time at which stress relaxation begins, σ_∞, the limiting stress, and, by plotting ln $(\sigma - \sigma_\infty)$ vs $(t - t_f)$, an estimate for τ. The subsequent application of nonlinear (Marquardt) regression to the stress data, following the form of eq 33, yields a value for A. Simple algebraic manipulation of A, τ, and σ_∞ therefore returns:[24]

$$E_1 = \frac{1}{\tau \dot{\epsilon}_0}\left(A + \frac{\sigma_\infty \tau}{t_f}\right) \quad (34)$$

$$E_2 = \frac{\sigma_\infty}{\dot{\epsilon}_0 t_f}\left(1 + \frac{\sigma_\infty \tau}{A t_f}\right) \quad (35)$$

and

$$\eta = \frac{1}{\epsilon_0}\left(A + \frac{2\sigma_\infty \tau}{t_f} + \frac{\sigma_\infty^2 \tau^2}{A t_f^2}\right) \quad (36)$$

as estimates for substitution into the equational definition (eq 24) for the relaxation function.

Solution of Viscoelastic Case Equations—The premise of this study was to mathematically describe the link between applied load and the evolution of particle–particle contact area between spherical bodies during densification. In this way, the material response may be incorporated in the mathematical description. The experimental data described in the preceding sections measured specific contact area growth resulting from specified applied loads, which then serve as input boundaries for the mathematical relation described in the set of eqs 27–30.

Decomposition of the stress–time curves into applied periods of strain allowed for the estimation of the variables comprising the relaxation modulus operator ($\Psi(t)$, eq 24). The radius of the contacting area (eq 28) was then to be solved for a prescribed loading force–time with substitution of this viscoelastic operator $\Psi(t)$. Application of integration by parts (see *Appendix IV*) provided a simplified form of the equation

$$a^3(t) = \frac{3}{8}\pi R\left\{\frac{P(t)}{E_1} - \left(\frac{1}{E_1} + \frac{1}{E_2} - \frac{1}{E_2}e^{-\frac{tE_2}{\eta}}\right)P_0\right\} + \int_0^t \frac{P(t')}{\eta} e^{-\frac{(t-t')E_2}{\eta}} dt' \quad (37)$$

which was then processed using the numerical quadrature algorithm of a commercial high-performance numeric computation and visualization software program (MATLAB, The MathWorks, Inc., Natrick, MA). The initial processing was performed with a Fortran numerical quadrature subroutine,[22] which was cumbersome compared with the speed with which the commercial form using a recursive adaptive Newton-Cotes 8 panel rule was able to ameliorate the calculations.

A best-fit polynomial form for the contact area–time description was then returned as input into the equation form describing the pressure distribution within the sphere. Equations 29–30 were likewise simplified to

$$p(r,t) = \frac{8}{\pi R}\left\{(a^2(t) - r^2)^{1/2}E_1 - (a_0^2 - r^2)^{1/2}\frac{(E_1^2 e^{-\frac{t}{\tau}} + E_1 E_2)}{E_1 + E_2} - \int_0^t (a^2(t') - r^2)^{1/2} \cdot \frac{E_1^2}{(E_1 + E_2)\tau} e^{-\frac{(t-t')}{\tau}} dt'\right\} \quad (38)$$

where $\tau = \eta/(E_1 + E_2)$, and processed in MATLAB.

Results and Discussion

The primary motivation for studying the particle level contact was the need to ascertain a time-dependent material function for subsequent modeling analysis. With the focus of this study centered on the interaction zone between two particles under mutual deformation, the loading force under which our experimental matrixes were subjected and the resultant experimental area growths were monitored. The applied loading force curves are depicted in Figures 7 and 8 inclusive. Each displayed curve represents the average of several large experimental datasets; the experimental standard deviation for selected points along a curve are shown in Figure 9 for clarity. In accordance with the geometry of the load application, the applied force experienced within the contact zone matches that which was applied externally through the Instron apparatus. The effect of the applied nominal strain rates is clearly shown in the force versus time series of Figure 7. As expected, the time to achieve a defined maximum load was inversely proportional to the crosshead speed, and, within experimental error, the ratio of such times mirrored the ratios of the respective strains (1:2:5:10) applied.

Force–time curves were replotted in Figure 8 for each nominally applied strain rate. Within experimental error, then, the maximum load level itself may be inferred as a function of the time under which the cylinders are compressed and hence not wholly independent of the applied rate of strain. The fitted coefficients for the power form of the force–time curves are summarized in Table 1. From multiple regression analyses, the prescribed loading force–time, $P(t)$, rate dependence may be embodied in the equational form

$$P(t) = (2.859 \times 10^{-2}\dot{\epsilon} + 3.233 \times 10^{-3}\dot{\epsilon}^2)(t - \text{lagtime})^{1.1} \quad (39)$$

where $\dot{\epsilon}$ is the applied strain rate. The value $R^2_{adj} = 98.34$, SE = 0.0424, mean absolute error equals 0.0246, and the mean square residual is 1.802×10^{-3}.

Radial contact growth curves derived from triplicate runs are displayed with error bars representing the replicate variability in Figures 10a–d inclusive. The effect of the applied nominal strain rates is clearly revealed in the sequence of plots where the strain rate differs in achieving a standard maximum load. This rate dependence is analogous to that which was manifest in the force–time series; that is, the time required to attain a specified dilation was inversely proportional to the applied crosshead speed and, within experimental error, the ratio of these times were roughly 1:2:5:10.

By replotting the radial growth curves in Figures 11a–d for each nominally applied strain rate, the effect of the maximum load level achieved is evidently once again a function of the time spent under compression. Each curve series held at a constant strain rate resembles a collinear plot within experimental error. The errors associated with higher strain rates are larger in relation to the points shown at lower strains because there is a finite time required to measure, process, and handle the photographs capturing the changing radial area.

The experimental radial growth data curves were subjected to simple regression fitting (minimization of least squares), and the coefficients of the normalized radial growth, $a(t)$, fitted to the square root of time are tabulated in Table 2.

The solution of the constitutive differential equation describing the behavior during a stress relaxation experiment to yield the relaxation function parameters is not an easy task. For simple models comprised of one to three

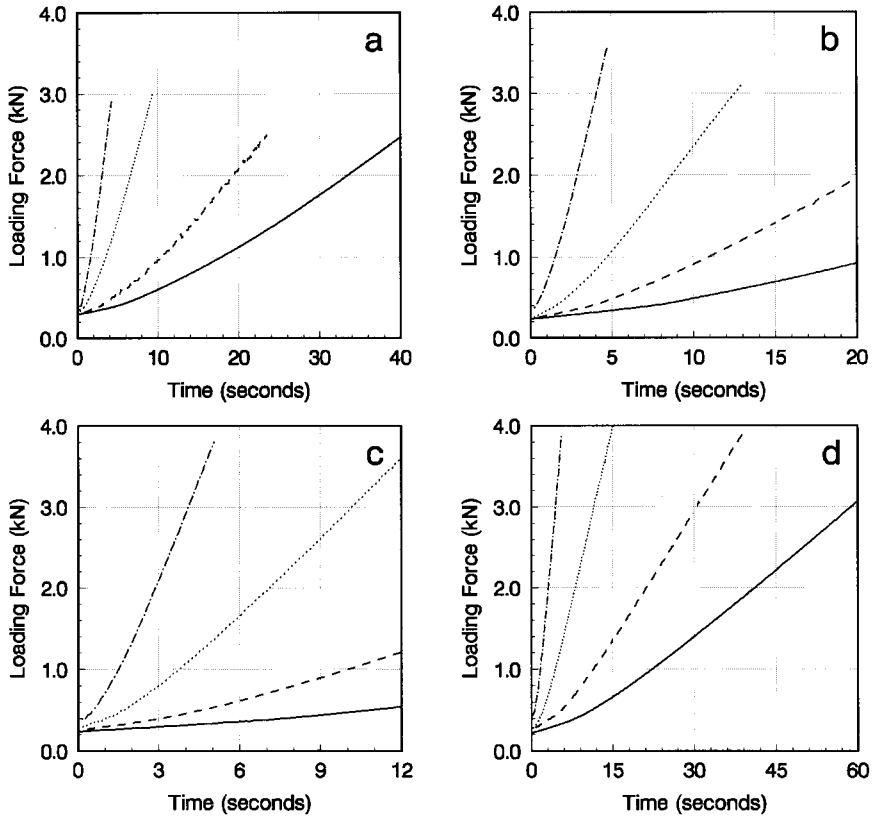

Figure 7—Applied load–time curves for various strain rates imposed on the mutually indenting matrixes: to a maximum load level of (a) 3.0 kN; (b) 3.5 kN; (c) 4.0 kN; and (d) 4.5 kN. Key: (—) 1 mm/min; (– – –) 2 mm/min; (•••) 5 mm/min; (- - -) 10 mm/min.

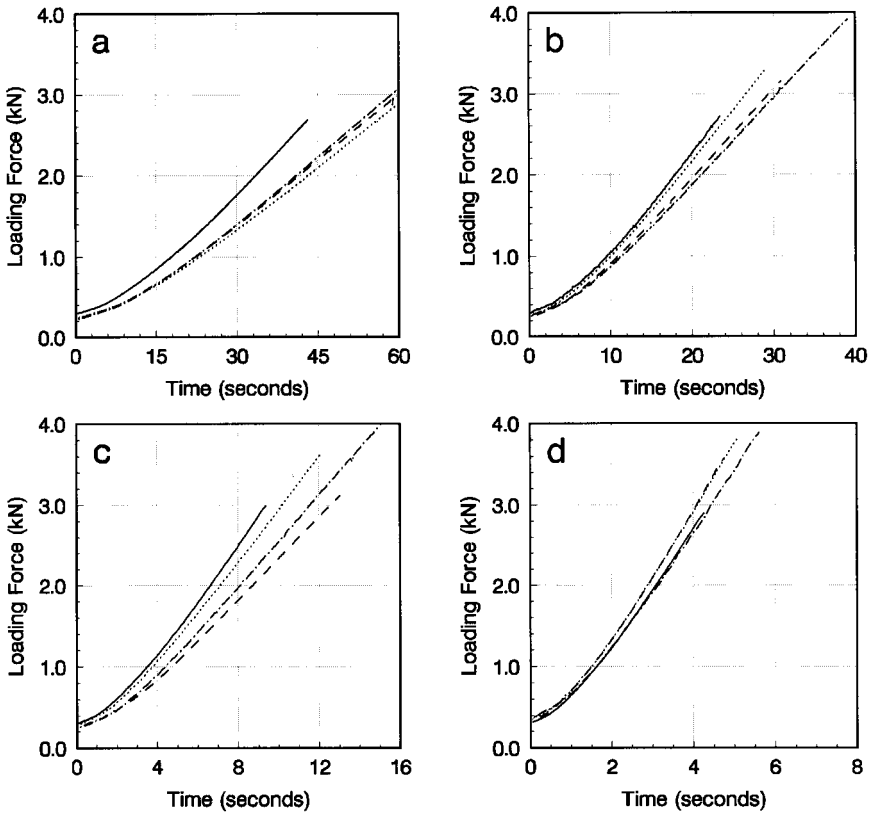

Figure 8—Applied load–time curves at specified strain rates and various loading levels for the cylinders in crossed compaction: loading at (a) 1 mm/min; (b) 2 mm/min; (c) 5 mm/min; and (d) 10 mm/min. Key: (—) 3.0 kN; (– – –) 3.5 kN; (•••) 4.0 kN; (- - -) 4.5 kN.

elements, the relaxation function may be formulated using hybrid parameters, which also allows a valid conversion to the creep compliance at the same point and at the same time.[25] In more complex models, the relaxation force equalizes differently in time and direction using parts of the springs, dashpots, and Kelvin elements differentially

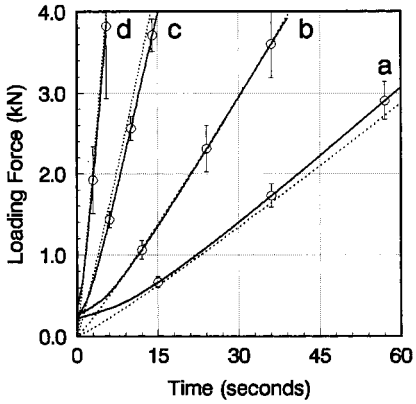

Figure 9—Loading force–time plots of the results obtained from use of the applied strain rates (a) 1 mm/min, (b) 2 mm/min, (c) 5 mm/min, and (d) 10 mm/min, to a maximum of 4.5 kN. Displayed in dotted form are the resultant curves predicted for the prescribed loading at these various strain rates. Selected experimental datapoints depicting the standard deviations between triplicate runs are highlighted.

Table 1—Force–Time Loading Phase of PMMA/CoMAA Matrices[a]

strain rate (mm/min)	maximum load (kN)	average coefficient of fit ($\times 10^{-2}$)	average lag time (s)
1	3.0	4.239 ± 0.57	34.17 ± 3.22
1	3.5	3.431 ± 0.14	19.74 ± 0.10
1	4.0	3.288 ± 0.62	21.12 ± 0.76
1	4.5	3.370 ± 0.35	19.49 ± 1.38
2	3.0	8.382 ± 0.81	13.72 ± 5.16
2	3.5	7.250 ± 0.77	11.00 ± 0.47
2	4.0	8.047 ± 1.71	13.28 ± 4.43
2	4.5	6.966 ± 1.02	9.990 ± 1.35
5	3.0	25.28 ± 0.58	7.040 ± 0.19
5	3.5	18.49 ± 3.37	4.300 ± 0.47
5	4.0	23.36 ± 2.97	4.000 ± 0.34
5	4.5	20.13 ± 1.44	4.460 ± 1.17
10	3.0	58.69 ± 4.32	3.410 ± 0.21
10	3.5	62.33 ± 2.23	2.820 ± 0.93
10	4.0	59.68 ± 4.72	2.330 ± 1.17
10	4.5	58.20 ± 15.95	2.520 ± 1.01

[a] $P(t)$ = coefficient*(t – lag time)$^{1.1}$. Average fitted coefficients reported are calculated from triplicate runs in each case. Standard deviations reported reflect the matrix-matrix variability.

until a forceless condition arises. Consequently, in the time-dependent domain, no simple relation between the creep compliance and the relaxation function may be found.[25]

Extraction of the relaxation function parameters, based on a standard three-element model from compaction load-time experiments, was preferred over the use of traditional measured creep tests over long times and elevated temperatures. As previously inferred, such tests would necessitate recasting specimen geometry or induce unwonted alterations in the material microstructure. A method used in material science to evaluate the viscosity and the two elastic modules of a three-parameter model during a combined experiment consisting of deformation with a constant strain rate followed by stress relaxation was adopted as a suitable means of evaluation of the PMMA/coMAA $\Psi(t)$ parameters. The crossed cylinder compactions performed consisted of the prerequisite deformation, load-time monitoring under a set crosshead speed, and relaxation monitoring under constant strain. The assumption of the equivalence of a constant crosshead speed with a constant nominal strain rate is a best first approximation. This method is consistent with an engineering definition of strain[26] ($\epsilon = \Delta l/l_0$, where Δl is the change in distance, l is the postfacto length, and l_0 is the original specimen length) rather than that of true strain [$\epsilon_t = \int dl/l_0 = \ln(l/l_0)$].

Table 2—Normalized Radial Growth with Time during Loading Phase of PMMA/CoMAA Matrices[a]

strain rate (mm/min)	maximum load (kN)	intercept of fit ($\times 10^{-2}$)	coefficient of fit ($\times 10^{-1}$)
1	3.0	–0.198 ± 2.0	1.201 ± 0.04
1	3.5	–8.500 ± 3.0	1.349 ± 0.05
1	4.0	–2.723 ± 1.5	1.256 ± 0.02
1	4.5	–14.47 ± 2.2	1.416 ± 0.03
2	3.0	–8.836 ± 3.9	1.845 ± 0.11
2	3.5	–11.54 ± 2.8	1.884 ± 0.07
2	4.0	–16.50 ± 3.6	1.955 ± 0.09
2	4.5	–11.55 ± 2.6	1.862 ± 0.05
5	3.0	–18.68 ± 7.2	3.679 ± 0.29
5	3.5	–6.614 ± 2.0	3.163 ± 0.09
5	4.0	–18.06 ± 3.1	3.528 ± 0.13
5	4.5	–5.969 ± 4.4	3.255 ± 0.16
10	3.0	–2.216 ± 7.0	5.171 ± 0.33
10	3.5	–4.783 ± 5.4	6.477 ± 0.25
10	4.0	–3.845 *	5.682 *
10	4.5	–2.135 *	5.312 *

[a] $a(t)$ = intercept + coefficient × $\sqrt{t}$. Average fitted coefficients reported are calculated from triplicate runs in each case. Standard errors reported reflect the matrix–matrix variability.

Others[25] have used solely numerical means for decomposing tabletting load–time curves. In both convolution and deconvolution processes of estimating viscoelastic model parameters, the numerical stability of the regression methods are problematic. The limited accuracy of the numerical transactions and the uncertainty of the initial condition estimates necessitates validation with well-defined, known theoretical material data. This necessity is especially true in the case of powder-type consolidation because volume reduction itself augments viscoelastic features.[25]

Figure 12 serves to illustrate the use of the decomposition method for the determination of the three-parameter viscoelastic terms for one specific case. The procedure is visually elucidated in terms of the decomposition of the stress relaxation curve into components in the development and provides an example of the nonlinear regression analysis used to determine the estimates in the summation process.

The derived parameters required for the relaxation modulus calculation are then summarized in Tables 3 and 4 per the method already described. These parameters serve as input variables in merely defining the viscoelastic operator over a limited time frame and by no means can be used to define $\Psi(t)$ over the time spectrum in its entirety.

Evaluation of the relaxation modulus (eq 24) with the parameters derived in Table 4 is shown in Figure 13. In physical terms, the relaxation modulus represents the time-dependent analogue of the equilibrium shear modulus, which in itself is a ratio of a stress to a corresponding strain measured in an experiment with a specific time pattern. The shape and magnitude of the log–log plots are consistent with that expected for an un-cross-linked polymer network of high molecular weight:[18] at short times, $\Psi(t)$ approaches a limiting value that represents the rigidity of the chain in the absence of backbone rearrangements, and at long times, $\Psi(t)$ falls rapidly for the un-cross-linked networks and eventually vanishes. A mechanical model analogue would translate this behavior as the relaxation of all the springs in an array. Alternatively, in molecular terms, this configuration corresponds to the resumption of random average configurations by the macromolecular coils that have been divested from the constraints originally imposed on them. The external dimensions of the sample in question may remain deformed at long times during this

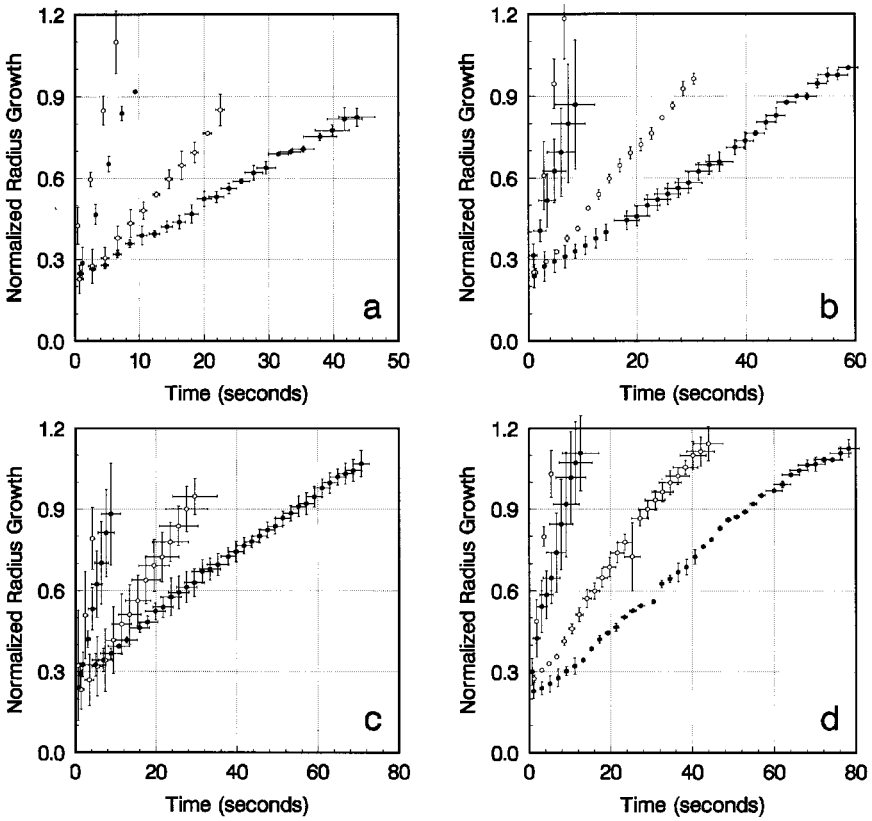

Figure 10—Averaged radial contact growth-time series for various strain rates measured concomitantly: to a maximum load level of (a) 3.0 kN; (b) 3.5 kN; (c) 4.0 kN; and (d) 4.5 kN.

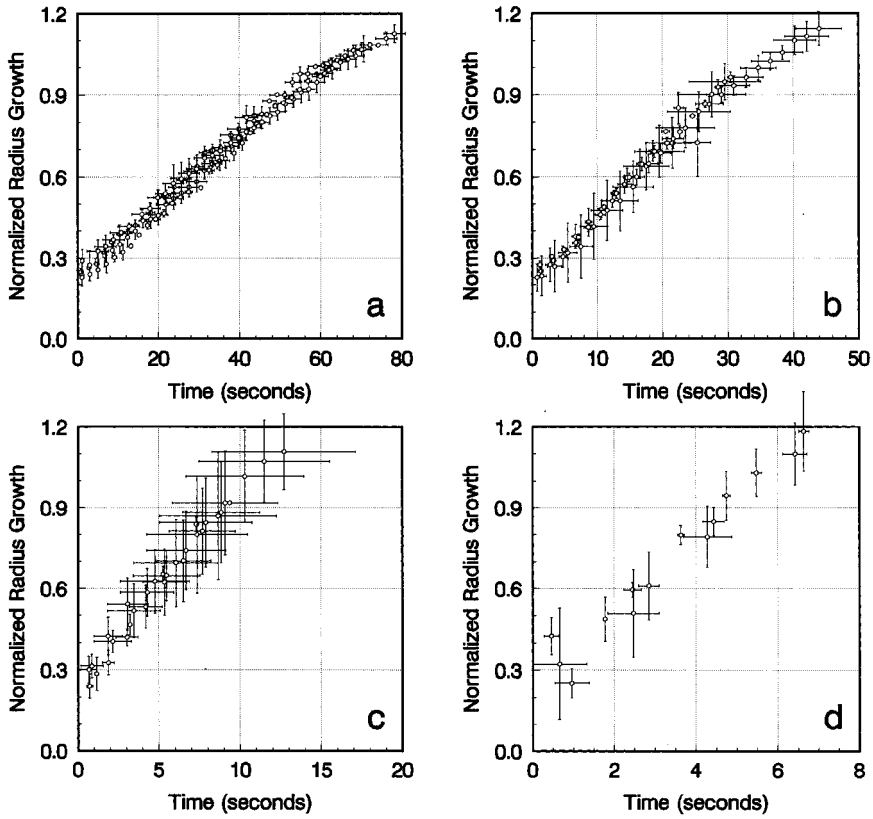

Figure 11—Radial contact growth–time series for the cylinders in crossed compaction at specified strain rates: loading at (a) 1 mm/min; (b) 2 mm/min; (c) 5 mm/min; and (d) 10 mm/min.

resumption of molecular motion; the residual deformation is the result of the flow contribution to what is essentially a creep experiment.

The magnitude of the compressionally derived modulus depicted in Figure 13 is lower than that reported for PMMA[14] achieved by tension experimentation. This dif-

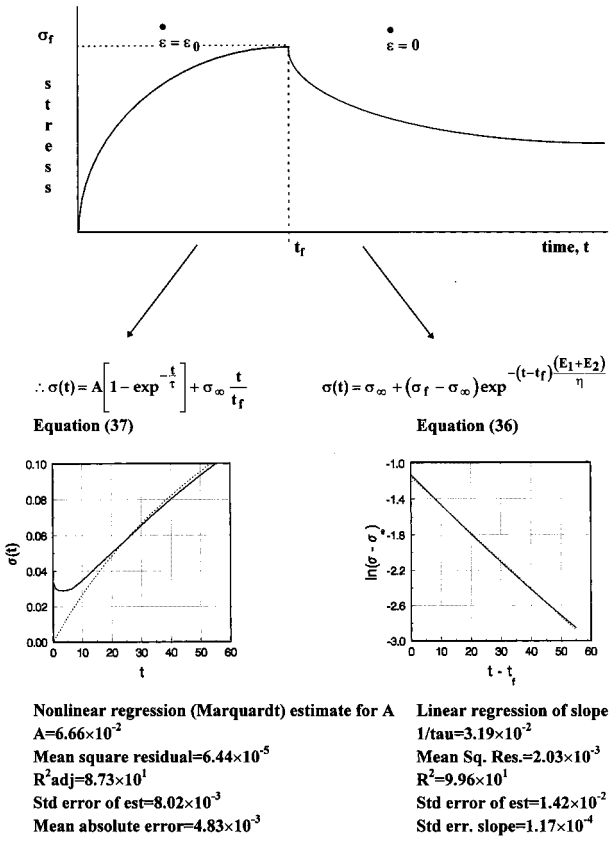

Figure 12—Schematic of the decomposition of the stress–time curve for the case of a load level of 3.0 kN achieved through loading at 1 mm/min. Evaluation of the viscosity and modulus components of a three-parameter model follows that described by Hsueh.[23]

ference is not unexpected, because of the experimental configurational differences and the differences between the two experimental time patterns. At intermediate times depicted in each curve of the figure, the stress shown gradually falls as the distortion of the chain backbones compensates through Brownian motion; segments would adjust first with respect to other closely neighboring segments and then with respect to those farther removed. The modulus falls off sharply thereafter in the region time scale of the terminal zone.

The time dependent operator $\Psi(t)$ displays the effects of the applied strain rates 1, 2, 5, and 10 mm/min shown through the superposition of curves a−d. The trend is in accord with the anticipated rate effect, that is, the inflection time marking the terminal zone is abbreviated with higher strain rates, while the inflection times are elongated with lower strains.

The parameters tabulated in Table 4 served as input for the calculation of the relaxational modulus and thereby the predicted radial contact growth for a prescribed load−time application. Numerical quadrature of the transformed eq 37 predicts a resultant contact growth that has been superimposed on the experimental dataset in Figure 14. The predicted curves are further tabulated using simple least squares regression in Table 5. Although the predicted curve lies within the range of experimental error, deviation from the measured growth may be due to error in the steps taken for the approximation of the specific relaxational modulus form. Indeed, assessing the fit of the predicted curves to this experimental set would not be a valid means of evaluating the utility of the model form as a predictive tool. An independent particle densification series based on stepped load, which was not itself used in the evaluation of the stress relaxation curves from which the relaxation operator was interpolated, would be required; such an assessment will form the basis for subsequent study.

In assessing the viscoelastic operator parameters derived in Table 4, it is clear that the value of the arbitrary maximum load level at which replicate runs were held is a complex function of the time under which loading occurs in a fashion similar to that deduced for load−time and radial growth−time curves. The nominal strain rate under which the matrixes were subjected serves as a better independent measure of the time-dependent behavior of each of the modulus parameters that comprise the $\Psi(t)$ operator. Multiple regression analysis of these tabulated parameters offers a best fit for E_1, E_2, and η when stratifying for specific load levels achieved. For the 4.5 kN levels, as an example,

$$E_1 = 1.70 \times 10^{-3} + 1.60 \times 10^{-3}\dot{\epsilon} - 4.47 \times 10^{-4}\dot{\epsilon}^2 + 3.62 \times 10^{-4}\dot{\epsilon}^3 - 5.58 \times 10^{-7}\dot{\epsilon}^4$$

$$E_2 = 5.21 \times 10^{-4} + 4.28 \times 10^{-5}\dot{\epsilon} - 5.69 \times 10^{-5}\dot{\epsilon}^2 + 6.96 \times 10^{-6}\dot{\epsilon}^3 - 1.15 \times 10^{-7}\dot{\epsilon}^4$$

$$\eta = 5.30 \times 10^{-1} - 1.71 \times 10^{-1}\dot{\epsilon} + 3.67 \times 10^{-2}\dot{\epsilon}^2 - 2.91 \times 10^{-3}\dot{\epsilon}^3 + 4.47 \times 10^{-5}\dot{\epsilon}^4$$

represents a parametrization set that may be used for interpolative prediction within the experimental boundaries delineated in the origin of the dataset. The values of E_1, E_2, and η represent theoretical estimates of the stiffness and flowability of the viscoelastic material. Together, these values form a mathematical construct of the viscoelastic behavior of the material that allows for prediction of the material behavior under different testing conditions. In a viscoelastic body, all of the stresses, strains, and displacements occurring are time dependent, whereas in an elastic solid under constant load, these parameters are independent of time. The values of these spring moduli and dashpot viscosity may provide an estimate of elastic parameters that represent the limiting case of a viscoelastic material. This theory is elucidated in *Appendix V*. Obviously, caution must be exercised in attempting to extrapolate beyond the strain rates prescribed because the size of the dataset lends insufficient power to that function.

The pressure distribution within the two mutually indenting viscoelastic three-parameter model spheres was also found by substituting the relaxation modulus function solved from eq 24 and $a(t)$ as derived from eq 37 into eq 38 and performing the integrations. The computations were carried out for each of the cases indicated in Table 4; the results are plotted in Figures 15a and b for the case of 4.5 kN at both 1 and 10 mm/min loading. These simplified sketches display a two-dimensional projection of the matrix solution which forms a three-dimensional contour (radius, time) in the Cartesian plane. From this schematic, one may infer that immediately following load application, there is an instantaneous elastic response from which the initial contact radius arises. This contact size then grows with time as discussed in preceding sections. It is apparent that the pressure distribution is similar to the Hertz elastic form given by

$$p = p_0\left(1 - \left(\frac{r}{a}\right)^2\right)^{-1/2} \qquad (40)$$

in which the maximum pressure is in the center of the contact area. As time progresses during loading, the balance of relaxation, contact, and load growth favors an

Table 3—Calculation of Material Viscoelastic Parameters Per Method of Hsueh[23]

4 × 4 matrix element code	peak time t_f (s)	relaxation stress σ_∞ (MPa) ($\times 10^{-2}$)	tau^{-1} ($\times 10^{-2}$)	coefficient A ($\times 10^{-2}$)	E_1 ($\times 10^{-3}$)	E_2 ($\times 10^{-3}$)	η ($\times 10^{-1}$)
11a	54.87	4.670	3.186 (0.01)	6.664 (0.80)	2.974	1.192	1.308
11b	46.00	6.716	5.794 (0.02)	4.567 (0.84)	4.107	2.265	1.100
11c	43.01	7.448	7.769 (0.06)	3.998 (0.82)	4.838	2.697	0.970
12a	64.31	2.359	1.443 (0.01)	20.03 (0.97)	3.258	0.413	2.544
12b	68.09	2.683	1.545 (0.01)	17.46 (0.91)	3.092	0.452	2.293
13a	70.16	3.684	0.909 (0.002)	32.61 (1.37)	3.489	0.618	4.519
13b	105.67	2.967	1.054 (0.002)	28.96 (1.18)	3.332	0.307	3.453
13c	75.9	2.707	0.639 (0.001)	24.00 (1.34)	1.890	0.440	3.656
14a	91.44	3.291	0.804 (0.001)	27.62 (1.16)	2.580	0.418	3.731
14c	77.63	3.981	0.928 (0.001)	29.13 (1.30)	3.215	0.610	4.124
21a	25.66	8.042	11.46 (0.09)	5.224 (0.85)	4.560	2.388	0.606
21b	23.37	4.512	3.359 (0.01)	17.57 (1.10)	3.916	1.281	1.547
21c	27.61	5.568	7.219 (0.04)	7.890 (1.00)	3.856	1.365	0.723
22b	37.49	2.959	1.517 (0.006)	46.99 (1.36)	3.959	0.438	2.899
22c	34.35	2.335	1.200 (0.005)	43.81 (1.33)	2.969	0.384	2.793
22d	30.76	3.289	1.416 (0.004)	40.12 (1.33)	3.376	0.635	2.832
23a	34.74	2.614	1.293 (0.003)	38.14 (1.11)	2.842	0.434	2.534
23c	28.79	11.09	14.70 (0.20)	5.407 (0.86)	5.901	2.861	0.596
23d	45.95	1.502	0.827 (0.001)	44.68 (1.03)	2.012	0.178	2.646
24a	45.69	3.541	1.344 (0.004)	44.26 (1.47)	3.362	0.438	2.827
24b	50.92	2.161	0.843 (0.001)	58.80 (1.72)	2.690	0.230	3.465
24c	38.91	4.266	1.566 (0.002)	46.24 (1.73)	4.168	0.631	3.065
31a	9.54	5.072	18.23 (0.12)	6.809 (0.93)	3.545	1.519	0.278
31b	9.27	3.664	11.39 (0.09)	11.40 (1.00)	3.387	1.031	0.388
31c	9.27	2.247	5.632 (0.02)	22.37 (1.10)	3.005	0.578	0.636
32a	18.12	0.685	1.211 (0.002)	79.53 (1.79)	2.003	0.079	1.718
32b	13.62	0.740	1.058 (0.002)	135.3 (1.87)	2.971	0.113	2.915
32c	12.95	1.029	1.425 (0.003)	109.1 (1.85)	3.269	0.167	2.410
33a	11.92	1.102	1.660 (0.004)	90.27 (1.62)	3.182	0.196	2.035
33b	15.19	0.308	0.639 (0.002)	165.1 (1.52)	2.152	0.041	3.430
33c	12.89	1.358	2.294 (0.006)	59.04 (1.61)	2.920	0.227	1.372
34a	16.54	0.975	1.111 (0.002)	123.8 (2.03)	2.869	0.123	2.694
34b	18.82	0.788	1.021 (0.002)	113.8 (1.97)	2.408	0.087	2.443
34c	16.25	0.946	1.205 (0.002)	117.2 (2.14)	2.939	0.121	2.540
41b	4.69	2.982	13.26 (0.08)	19.96 (0.97)	3.282	0.788	0.307
41c	4.18	1.809	7.021 (0.03)	45.45 (1.11)	3.624	0.491	0.586
42a	4.75	5.175	25.50 (0.25)	10.98 (0.87)	3.888	1.514	0.212
42c	4.63	2.411	8.886 (0.03)	31.88 (1.04)	3.354	0.616	0.447
42d	4.85	2.428	12.03 (0.06)	25.19 (1.00)	3.532	0.583	0.342
43a	5.12	5.662	24.86 (0.25)	11.24 (0.92)	3.901	1.543	0.219
43c	5.69	2.797	12.78 (0.08)	25.36 (1.00)	3.733	0.566	0.336
43d	5.71	5.986	38.39 (0.33)	7.463 (0.78)	3.914	1.432	0.139
44a	8.91	2.309	7.612 (0.03)	23.30 (1.10)	2.033	0.297	0.306
44b	5.61	8.089	40.28 (0.31)	8.776 (1.14)	4.976	2.030	0.174
44c	5.51	3.954	14.84 (0.14)	23.12 (1.29)	4.148	0.868	0.338

Table 4—Calculation of Material Viscoelastic Parameters[a]

strain rate (mm/min)	maximum load (kN)	average E_1 ($\times 10^{-3}$)	average E_2 ($\times 10^{-3}$)	average η ($\times 10^{-1}$)
1	3.0	3.973 ± 0.94	2.052 ± 0.78	1.126 ± 0.17
1	3.5	3.175 ± 0.12	0.433 ± 0.03	2.418 ± 0.18
1	4.0	2.904 ± 0.88	0.455 ± 0.16	3.873 ± 0.57
1	4.5	2.897 ± 0.45	0.514 ± 0.14	3.927 ± 0.28
2	3.0	4.111 ± 0.39	1.678 ± 0.62	0.959 ± 0.51
2	3.5	3.435 ± 0.50	0.486 ± 0.13	2.841 ± 0.05
2	4.0	3.585 ± 2.05	1.158 ± 1.48	1.925 ± 1.15
2	4.5	3.407 ± 0.74	0.433 ± 0.20	3.119 ± 0.32
5	3.0	3.312 ± 0.28	1.043 ± 0.47	0.434 ± 0.18
5	3.5	2.748 ± 0.66	0.119 ± 0.04	2.348 ± 0.60
5	4.0	2.751 ± 0.54	0.155 ± 0.10	2.279 ± 1.05
5	4.5	2.739 ± 0.29	0.110 ± 0.02	2.559 ± 0.13
10	3.0	3.453 ± 0.24	0.640 ± 0.21	0.446 ± 0.20
10	3.5	3.591 ± 0.27	0.905 ± 0.53	0.333 ± 0.12
10	4.0	3.849 ± 0.10	1.180 ± 0.54	0.232 ± 0.10
10	4.5	3.719 ± 1.52	1.065 ± 0.88	0.273 ± 0.09

[a] Average fitted coefficients reported are calculated from triplicate runs in each case. Standard deviations reported reflect the matrix–matrix variability.

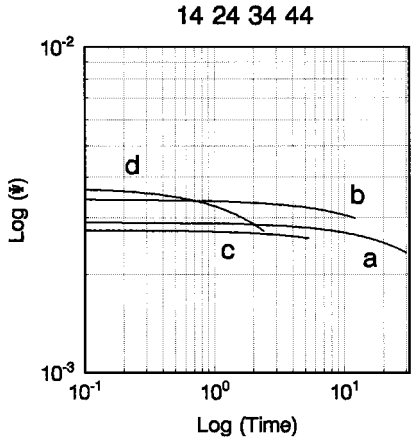

Figure 13—log–log plot of the relaxational modulus–time curves calculated for compaction at the rates of loading at (a) 1 mm/min, (b) 2 mm/min, (c) 5 mm/min, and (d) at 10 mm/min, to a maximum load of 4.5 kN.

expanding pressure distribution. Variation in the loading rate results in a marginally greater magnitude of pressure distributed in a similar fashion. The time-dependent effect, therefore, would appear to consist of the growth in the contact from its initial to its final size; the stresses at any instant in the process being distributed according to elastic theory.

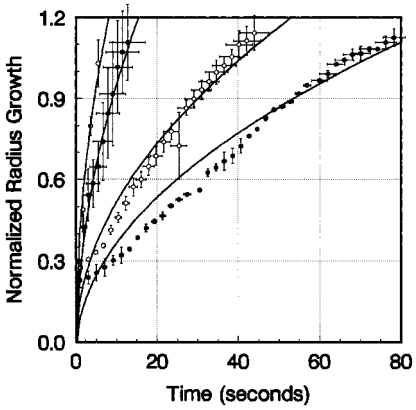

Figure 14—Predicted radial growth curves for various strain rates imposed on the compact to a loading level of 4.5 kN: loading at (a) 1 mm/min, (b) 2 mm/min, (c) 5 mm/min, and (d) 10 mm/min.

Table 5—Predicted Normalized Radial Growth with Time During Loading Phase of PMMA/coMAA Matrices[a]

strain rate (mm/min)	intercept of fit ($\times 10^{-2}$)	coefficient of fit ($\times 10^{-2}$)
1	–4.005 (0.25)	12.846 (0.06)
2	–0.741 (0.10)	16.577 (0.04)
5	–7.281 (0.30)	32.381 (0.17)
10	–0.941 (0.18)	42.564 (0.15)

[a] Average fitted coefficients and standard errors reported are calculated for a maximum loading level of 4.5 kN.

Conclusions

The present investigation was undertaken to examine the basic unit of densification: the particle–particle interaction. Emphasis was placed on the contact interface between two spheres under compression as interparticulate bonding inherently occurs whenever an area of true contact is established between two solids; the interfacial energy is always less than the surface energy of the two surfaces which form the interface. The degree of cohesion within a tablet was assumed to be largely governed by the magnitude of this true interparticle contact area created during densification.

The interfacial description of two linearly viscoelastic spheres in normal contact was described mathematically by replacing the elastic constant of the elastic solution by the integral operator from the viscoelastic stress–strain relations. An explicit relation was delineated between contact area evolution and the applied or prescribed contact force in a 4 × 4 matrix of varying strain and load level. The analysis of the extended Hertzian solution with experimentally determined input parameters yielded two-dimensional surface plots which map the evolution of these variables of local contact force, area growth, and pressure functions with time and applied strain rate at specified maximum loads. Within the context of the experimental time frame, these relations form the basis for the superposition of such contacts in summation over the entire powder bed.

By defining the contact between mutually indenting viscoelastic particles, the compact may ultimately be modeled as a collection of these particles in contact and in this way address the time-dependent response of materials to applied loads. This summation to describe a tabletting powder is the subject of the second paper in this series.

Acknowledgments

This work was abstracted in part from a dissertation submitted by S.L. to the Graduate School, University of Toronto, in partial fulfillment of the Doctor of Philosophy degree. The authors thank and acknowledge the financial assistance of MRC in the form of a grant (to W.D.H.) and a studentship (to S.L.) in supporting this study.

Appendix I

As the length of the cord $bc = 2r = 2a \cos\theta$, $r = a \cos\theta$ since $a \sin\theta = r \sin\psi$

$$a^2 \sin^2\theta = r^2 \sin^2\psi$$

$$a^2(1 - \cos^2\theta) = r^2 \sin^2\psi$$

$$a^2 - a^2 \cos^2\theta = r^2 \sin^2\psi$$

$$a^2 \cos^2\theta = a^2 - r^2 \sin^2\psi$$

$$\therefore a \cos\theta = \sqrt{a^2 - r^2 \sin^2\psi}$$

$$\therefore \text{area of circle} = \pi r^2 = \pi(a^2 - r^2 \sin^2\psi)$$

$$\therefore w = \frac{(1 - \upsilon^2)}{\pi E} q\pi \int_0^{\pi/2} (a^2 - r^2 \sin^2\psi)\mathrm{d}\psi$$

Appendix II

Pressure Applied to a Circular Region—When axisymmetrical pressure distributions of the form

$$q = q_0\left(1 - \frac{r^2}{a^2}\right)^n$$

are applied to a circular region of radius a, the displacements at surface points and the stresses at internal points due to this pressure distribution may be found in closed form.

In the particular case where $n = 1/2$, the pressure distribution is referred to as the "Hertz pressure" given by Hertz theory. This pressure is exerted between two frictionless purely elastic solids of revolution in contact.

As the total loading or compressive force, P, relates to this pressure, q, via

$$P = \int_0^a q(r) 2\pi r \mathrm{d}r$$

then

$$p = \frac{2\pi q_0}{a} \int_0^a (a^2 - r^2)^{1/2} r \mathrm{d}r$$

let $u = a^2 - r^2$, $\mathrm{d}u = -2r\mathrm{d}r$, $r\mathrm{d}r = -1/2\ \mathrm{d}u$, and $a^2 = u + r^2$

$$\therefore P = \frac{2\pi q_0}{a} \int_0^1 u^{\frac{1}{2}}\left(-\frac{1}{2}\right)\mathrm{d}u = \left[-\frac{2\pi q_0}{3a} u^{\frac{3}{2}}\right]_0^a = \left[-\frac{2\pi q_0}{3a}(a^2 - r^2)^{\frac{3}{2}}\right]_0^a = \frac{2}{3}\pi q_0 a^2$$

$$\therefore \text{force} \propto \text{maximum pressure}$$

$$\therefore q_0 = \frac{3P}{2\pi a^2}$$

Appendix III

Derivation of Simplified Three-Dimensional Form for Viscoelastic Constitutive Description[19]—When a problem has more than one stress component, then a generalization of the viscoelastic law to the three-dimensional form may be needed. If a viscoelastic material is

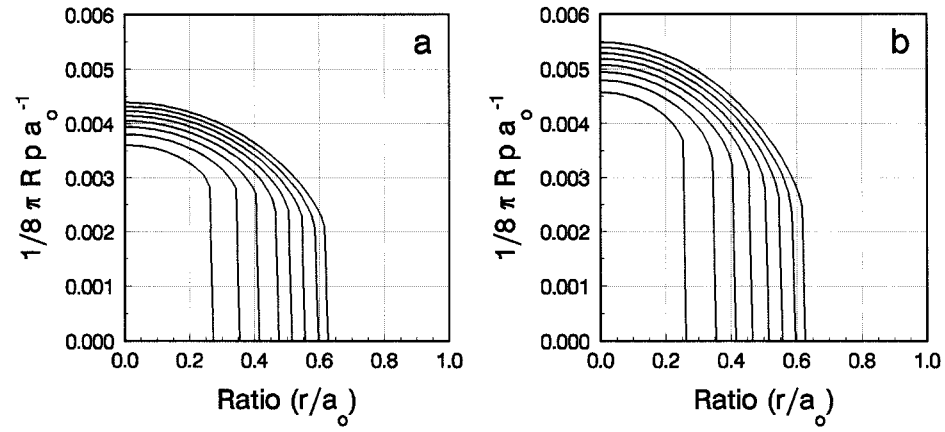

Figure 15—Solution of the pressure equations predicts a stress distribution similar to the elastic form. (a) two-dimensional surface contour plot of the pressure distribution for loading at 1 mm/min to the 4.5 kN level; and (b) loading at 10 mm/min to the 4.5 kN level.

isotropic, a hydrostatic stress must produce a dilatation and no distortion. The stress and strain are related by the differential equation

$$\sigma + p_1\dot{\sigma} + p_2\ddot{\sigma} + \ldots = q_0\epsilon + q_1\dot{\epsilon} + \ldots \qquad \text{(III.1)}$$

$$\left(\sum_0^m p_k \frac{\mathrm{d}^k}{\mathrm{d}t^k}\right)\sigma = \left(\sum_0^n q_k \frac{\mathrm{d}^k}{\mathrm{d}t^k}\right)\epsilon \qquad \text{(III.2)}$$

or, shorter, by

$$P''\sigma = Q''\epsilon \qquad \text{(III.3)}$$

On the other hand, if shear is present, then the shear strain coupled with isotropy of the material requires that

$$\left(\sum_0^{m'} p'_k \frac{\mathrm{d}^k}{\mathrm{d}t^k}\right)\hat{\sigma} = \left(\sum_0^{n'} q'k \frac{\mathrm{d}^k}{\mathrm{d}t^k}\right)\hat{\epsilon} \qquad \text{(III.4)}$$

or

$$P'\hat{\sigma} = Q'\hat{\epsilon} \qquad \text{(III.5)}$$

where $\hat{\sigma}$ and $\hat{\epsilon}$ correspond to the components of the stress and strain deviators.

The operator pairs P'', Q'', and P' and Q', which describe the viscoelastic material, are entirely independent of each other. To each pair, the relation stated in eq 23 or 24 is applicable for a standard three element model.[19] These operator pairs for different rheological models are also summarized in Flugge (Table 1.2; pp 22−23)[19] and in Muller (pp 108, 110, 112, 119, 121).[25]

In uniaxial tension, there is only one stress, σ_x; and strain has three components, the axial strain ϵ_x and the lateral contractions $\epsilon_y = \epsilon_z$. As the operators are assumed linear and time invariant, the commutative properties yields

$$(P''Q' + 2Q''P')\sigma_x = 3Q''Q'\epsilon_x \qquad \text{(III.6)}$$

$$(\mathrm{P}''\mathrm{Q}' - Q''P')\sigma_x = 3Q''Q'\epsilon_y \qquad \text{(III.7)}$$

for applied uniaxial stress. By analogy,

$$(Q''P' + 2P''Q')\epsilon_x = 3P''P'\sigma_x \qquad \text{(III.8)}$$

$$(Q''\mathrm{P}' - P''Q')\epsilon_x = 3P''P'\sigma_y \qquad \text{(III.9)}$$

follows for applied uniaxial strain (in stress relaxation experiments).

Equations III.6−III.9 serve as the viscoelastic equivalent of a complete statement of Hooke's law for uniaxial tension. Interpretation requires special choices for the operators.

As stated by Flugge (p 167),[19] although the shear deformation may be rather large, the change of volume measured by E is always very limited. It seems therefore, reasonable to neglect the latter completely and to assume $E = 0$. This corresponds to $P'' = 0$ and $Q'' = 1$. The constitutive equations for uniaxial stress in tension are then

$$2P'\sigma_x = 3Q'\epsilon_x \text{ and } -P'\sigma_x = 3Q'\epsilon_y \qquad \text{(III.10)}$$

and for applied uniaxial strain,

$$2Q'\epsilon_x = 3P'\sigma_x \text{ and } -Q'\epsilon_x = 3P'\sigma_y \qquad \text{(III.11)}$$

Appendix IV

$$a^3(t) = \frac{3}{8}\pi R\int_0^t\left\{\frac{1}{E_1} + \frac{1}{E_2}(1 - \mathrm{e}^{-\frac{(t-t')E_2}{\eta}})\right\}\frac{\mathrm{d}}{\mathrm{d}t'}P(t')\mathrm{d}t' \qquad (28)$$

integration by parts $uv - \int v\mathrm{d}u$: let

$$u = \frac{1}{E_1} + \frac{1}{E_2} - \frac{1}{E_2}\mathrm{e}^{-\frac{(t-t')E_2}{\eta}} \quad \therefore \mathrm{d}u = -\frac{1}{E_2}\cdot\frac{E_2}{\eta}e^{-\frac{(t-t')E_2}{\eta}}\mathrm{d}t'$$

$$\mathrm{d}v = \frac{\mathrm{d}}{\mathrm{d}t'}P(t')\mathrm{d}t' \quad \mathrm{v} = P(t')$$

$$\therefore a^3(t) = \frac{3}{8}\pi R\left[\left(\frac{1}{E_1} + \frac{1}{E_2} - \frac{1}{E_2}\,\mathrm{e}^{-\frac{(t-t')E_2}{\eta}}\right)(P(t'))\right]_0^t - \int\frac{P(t')}{-\eta}\mathrm{e}^{-\frac{(t-t')E_2}{\eta}}\mathrm{d}t'$$

$$\therefore a^3(t) = \frac{3}{8}\pi R\left\{\frac{P(t)}{E_1} - \left(\frac{1}{E_2} + \frac{1}{E_2} - \frac{1}{E_2}\mathrm{e}^{-\frac{tE_2}{\eta}}\right)P_0\right\} + \int_0^t\frac{P(t')}{\eta}\mathrm{e}^{-\frac{(t-t')E_2}{\eta}}\mathrm{d}t'$$

calculate $a(t)$ per given $P(t)$.

Similarly,

$$p(r,t) = \frac{4}{\pi R}\int_0^t\left\{E_1\mathrm{e}^{-\frac{t-t'}{\tau}} + \frac{E_1E_2}{E_1+E_2}(1 - \mathrm{e}^{-\frac{t-t'}{\tau}})\right\}\times \frac{\mathrm{d}}{\mathrm{d}t'}(a^2(t') - r^2)^{1/2}\,\mathrm{d}t'$$

where

$$\tau = \frac{\eta}{E_1 + E_2} \tag{30}$$

let

$$u = \frac{1}{E_1 + E_2} \cdot E_1^2 e^{-\frac{(t - t')}{\tau}} + \frac{E_1 E_2}{E_1 + E_2}$$

$$\therefore \mathrm{d}u = \frac{E_1^2}{(E_1 + E_2)\tau} \mathrm{e}^{-\frac{(t - t')}{\tau}} \mathrm{d}t'$$

and

$$\mathrm{d}v = \frac{\mathrm{d}}{\mathrm{d}t'}(a^2(t') - r^2)^{1/2} \mathrm{d}t' \quad \therefore v = (a^2(t') - r^2)^{1/2}$$

$$p(r,t) = \frac{8}{\pi R}\left\{(a^2(t) - r^2)^{1/2} E_1 - (a_0^2 - r^2)^{1/2} \frac{(E_1^2 e^{-\frac{t}{\tau}} + E_1 E_2)}{E_1 + E_2} - \right.$$

$$\left. \int_0^t (a^2(t') - r^2)^{1/2} \frac{E_1^2}{(E_1 + E_2)\tau} \mathrm{e}^{-\frac{(t - t')}{\tau}} \mathrm{d}t' \right\}$$

Appendix V

Derivation of Elastic Parameters as a Limiting Case[19]—In a viscoelastic body, all of the stresses, strains, and displacements occurring under load are time dependent. The elastic solid is then a limiting case of a viscoelastic material. The moduli of the springs of the rheological model do not correspond simply to Young's modulus because time, temperature, and stress dependence are overt considerations. If, for example, one considers a material tested in tension, the plot of the compliance would show that the ratio $\epsilon_x/-\epsilon_y$ varies with time. This time dependence indicates that the concept of Poisson ratios etc. are not very meaningful for a viscoelastic material.[19]

The linear elastic law (Hooke's law) in the form (III.1; see *Appendix III*) would render the four operators as multiplicative constants and the formulation of the stress deviation as[19]

$$\sigma_x = \frac{E}{(1 + \nu)(1 - 2\nu)}[(1 - \nu)\epsilon_x + \nu(\epsilon_y + \epsilon_z)] \tag{V.1}$$

The differential operators P and Q can be replaced by polynomials $\rho(s)$ and $\vartheta(s)$ in considering an elastic body, hence,[19]

$$\rho''(s)\bar{\sigma} = \vartheta''(s)\bar{\epsilon} \tag{V.2}$$

$$\rho'(s)\bar{\sigma} = \vartheta'(s)\bar{\epsilon} \tag{V.3}$$

where $\bar{\sigma}$ and $\bar{\epsilon}$ are the Laplace transforms of the time-dependent stresses and strains. These algebraic relations define the limits of their elastic counterparts if[19]

$$3K \rightarrow \frac{\vartheta''(s)}{\rho''(s)} \quad 2G \rightarrow \frac{\vartheta'(s)}{\rho'(s)} \tag{V.4}$$

$$E \rightarrow \frac{3\vartheta'\vartheta''}{2\rho'\vartheta'' + \vartheta'\rho''} \quad \nu \rightarrow \frac{\rho'\vartheta'' - \vartheta'\rho''}{2\rho'\vartheta'' + \vartheta'\rho''} \tag{V.5}$$

For a standard (three-parameter material), a reduced or effective modulus $E_R(t, \tau)$ offers estimates of an instantaneous $E_R(\tau_0,\tau_0)$ and an asymptotic modulus $E_R(\infty,\tau)$:[17]

$$E(\tau_0,\tau_0) = \frac{1}{E_1} \quad E(\infty,\tau_0) = \frac{E_1 E_2}{E_1 + E_2} \tag{V.6}$$

List of Symbols

$\dot{\epsilon}_0$	constant strain rate
$\dot{\epsilon}$	rate of strain
τ	interval within domain t, also designated $\eta/(E_1 + E_2)$
υ	Poisson's ratio
σ_∞	limiting stress during stress relaxation
$\Phi(t)$	creep function
$\epsilon(t)$	strain which varies with time
$\sigma(t)$	stress which varies with time
$\Psi(t)$	the relaxation modulus function, a viscoelastic operator
α, α_1, α_2	total distance of approach of two spheres, of each sphere designated 1 and 2
σ_f	stress at time corresponding to beginning of stress relaxation (strain rate = 0)
Δl	change in distance
ϵ_t	true strain
A	coefficient = $(E_1/E_1 + E_2)^2\eta\dot{\epsilon}_0$
a, $a(t)$	particle contact radius (radius of circular contact region) varying with time
E	elastic modulus
E_1, E_2, η	elastic moduli of the springs and viscosity coefficient of the dashpot of a standard rheological model
K, G	bulk, and shear modulus
$k_1 + k_2$	elastic constant term = $(1 - \upsilon^2)/\pi E$ upon substitution
l	length
l_0	original specimen length
$P(t)$	applied compressive force acting normal to the surface
p, $p(r,t)$	normal contact pressure which varies with contact radius and time
q, q_0	concentrated pressure, maximum pressure
r	distance from sphere center, x coordinate of point (r,z) of indenting sphere, $r \ll R$
R, R_1, R_2	radius of curvature, of the indenting spheres designated 1 and 2, respectively
t'	dummy time variable within interval t
t_f	time at which stress relaxation begins, total strain is held constant
w_1, w_2	deformation of sphere 1 and 2 owing to contact pressure
x, y, z	Cartesian coordinates
z_1, z_2	Cartesian coordinate projection of deforming surface points, designated 1 and 2

References and Notes

1. Hoag, S. W.; Rippie, E. G. Thermodynamic analysis of energy dissipation by pharmaceutical tablets during stress unloading. *J. Pharm. Sci.* **1994**, *83*, 903−908.

2. Paronen, P.; Ilkka, J. Porosity-pressure functions. In *Pharmaceutical powder compaction technology, Drugs and the pharmaceutical sciences series, 71*, Alderborn, G.; Nystrom, C., Eds.; Marcel Dekker: Inc.: New York, 1996; p 69.
3. Rippie, E. G.; Danielson, D. W. Viscoelastic stress/strain behavior of pharmaceutical tablets: analysis during unloading and postcompression periods. *J. Pharm. Sci.* **1981**, *70*, 476−481.
4. York, P. J. A consideration of experimental variables in the analysis of powder compaction behavior. *Pharm. Pharmacol.* **1979**, *31*, 244−246.
5. Duncan-Hewitt, W. C.; Papadimitriopoulos, E. Deformation kinetics of KBr crystals predict tablet stress relaxation. *J. Pharm. Sci.* **1994**, *83*, 91−95.
6. Celik, M.; Okutgen, E.; A feasibility study for the development of a prospective compaction functionality test and the establishment of a compaction data bank, *Drug Dev. Ind. Pharm.* **1993**, *19 (17&18)*, 2309−2334.
7. Pinto, J. F.; Podczeck, F; Newton, J. M.; Investigations of tablets prepared from pellets produced by extrusion and spheronisation. II. Modeling the properties of the tablets produced using regression analysis. *Int. J. Pharm.* **1997**, *152*, 7−16.
8. Rue, P. J.; Rees, J. E. Limitations of the Heckel relation for predicting powder compaction mechanisms. *J. Pharm. Pharmacol.* **1978**, *30*, 642−643.
9. Toure, P.; Puisieux, F.; Duchene, D.; Carstensen, J. T. Energy terms in tablet compression cycles. *Powder Technol.* **1980**, *26*, 213−216.
10. Johnson, K. L. *Contact mechanics*; Cambridge University: New York; 1985; p 542.
11. Timoshenko, S.; Goodier, J. N. *Theory of Elasticity*, third ed.; McGraw-Hill: New York; 1970; pp 409−420.
12. Gladwell,G. M. L. *Contact Problems in the Classical Theory of Elasticity*; Sijthoff and Noordhoff: Alphen aan den Rijn; 1980; p 95.
13. Lee, E. H.; Radok, J. R. M. The contact problem for viscoelastic bodies. *J. Appl. Mech.* **1960**, 438−444.
14. Lee, E. H.; Rogers, T. G. Solution of viscoelastic stress analysis problems using measured creep or relaxation functions. *J. Appl. Mech.* **1963**, 127−133.
15. Lee, E. H. Stress analyis in viscoelastic bodies. *Quart. Appl. Math.* **1955**, *13*, 183−190.
16. Radok, J. R. M. Viscoelastic stress analysis. *Quart. Appl. Math.* **1957**, *15*, 198−202.
17. Creus, G. J. Viscoelasticity- -Basic theory and applications to concrete structures. In *Lecture notes in engineering, 16*; Brebbia, C. A.; Orszag, S. A., Eds.; Springer-Verlag: New York, 1985; pp 18−42.
18. Ferry, J. D. *Viscoelastic Properties of Polymers*, second ed.; John Wiley & Sons: New York, 1970.
19. Flugge, W. *Viscoelasticity*, second ed., Springer-Verlag: New York, 1975; pp 22−23, 165−167.
20. Lum, S. K.; Duncan-Hewitt, W. C. A comparison of elastic moduli derived from theory, microindentation and ultrasonic testing. *Pharm. Res.* **1996**, *13*, 1739−1745.
21. Lum, S. K.; Duncan-Hewitt, W. C. Deformation kinetics analysis of polymeric matrixes. *Pharm. Res.* **1996**, *13*, 692−700.
22. Vetterling, W. T.;Teukolsky, S. A.;Press, W. H.;Flannery, B. P. *Numerical Recipes Example Book (Fortran)*, second ed.; Cambridge University: New York, 1992; p 245.
23. Hsueh, C.-H. Mathematical model of viscosity measurements for viscoelastic solids. *J. Am. Ceram. Soc.* **1986**, *69*, C48−C49.
24. Berg, G.; Grau, P. Estimating the viscosity of viscoelastic solids based on a three-parameter model. *J. Am. Ceram. Soc.* **1989**, *72*, 2187−2188.
25. Muller, F. Viscoelastic models. In *Pharmaceutical Powder Compaction Technology, Drugs and the pharmaceutical sciences series, 71*; Alderborn, G.; Nystrom, C., Eds.; Marcel Dekker: New York, 1996; pp 108−130.
26. Askeland, D. R. *The Science and Engineering of Materials*, PWS−Kent Publishing: Boston, 1984; pp 122, 128.

JS980010M